Inorganic Chemistry

Article

pubs.acs.org/IC

Structure, Optical Properties, and Magnetism of the Full $Zn_{1-x}Cu_xWO_4$ ($0 \leq x \leq 1$) Composition Range

Joseph E. Yourey, Joshua B. Kurtz, and Bart M. Bartlett*

Department of Chemistry, University of Michigan, 930 N. University Ave., Ann Arbor, Michigan 48109-1055, United States

Supporting Information

ABSTRACT: Microcrystalline and submicrometer powders of $Zn_{1-x}Cu_xWO_4$ ($0 \leq x \leq 1$) have been prepared by a solid-state synthesis from stoichiometric quantities of the constituent d-block metal oxide and tungsten oxide as well as from a Pechini sol–gel synthesis starting from the d-block metal nitrate and ammonium metatungstate. The stoichiometry of the product is confirmed by inductively coupled plasma-atomic emission spectrometry (ICP-AES) analysis. X-ray diffraction shows that for the entire range of compositions, a single-phase product crystallizes in the wolframite structure, with a symmetry-lowering transition from $P2/c$ to $P\bar{1}$ at $x = 0.20$, concomitant with the first-order Jahn–Teller distortion of Cu^{2+}. Far-IR spectroscopy corroborates that symmetry lowering is directly related to the tetragonal distortion within the CuO_6 octahedra, with the Zn–O A_u symmetry mode at 320 cm^{-1} ($x = 0$) splitting into two stretches at 295 and 338 cm^{-1} ($x = 0.3$). UV–vis–NIR spectroscopy shows an optical absorption edge characteristic of an indirect band gap that linearly decreases in energy from 3.0 eV ($x = 0$) to 2.25 eV ($x = 1$). SQUID magnetometry shows that $Zn_{1-x}Cu_xWO_4$ ($0.1 \leq x \leq 1$) has an effective moment of 2.30 ± 0.19 μ_B per mol copper, typical of Cu^{2+} in extended solids. For high concentrations of copper ($x \geq 0.8$), two transitions are observed: one at high-temperature, 82 K ($x = 1.0$) that decreases to 59 K ($x = 0.8$), and the Néel temperature, 23.5 K ($x = 1.0$) that decreases to 5.5 K ($x = 0.8$). For $x < 0.8$, no long-range order is observed. A physical 1:1 mixture of both $CuWO_4$:$ZnWO_4$ shows magnetic ordering identical to that of $CuWO_4$.

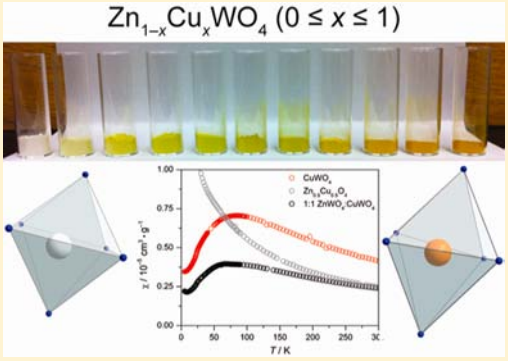

INTRODUCTION

Recent work in our laboratory has focused on $CuWO_4$ for water oxidation.[1] We find that a composite $CuWO_4$–WO_3 photoelectrode generates the highest photocurrent in KP_i buffer (pH 7). This compound displays an indirect band gap of 2.4 eV. The $CuWO_4$–WO_3 composite electrode shows an apparent quantum yield for water oxidation with simultaneous ferricyanide reduction of ∼0.04%.[2] Potential drawbacks of composite electrodes are that charge transfer at $CuWO_4$–WO_3 interfaces may be kinetically limiting, and identifying the absorptivity of and reaction kinetics of each constituent part is difficult. Therefore, we seek single phase mixed-metal materials in which to investigate carrier mobility and photoelectrochemistry.

To begin, we have prepared the series $Zn_{1-x}Cu_xWO_4$ in two ways: by traditional solid-state synthesis and, for the first time, by a sol–gel processing method which is amenable for spin-casting to form photoanodes. We focus on zinc analogues because zinc substitution for copper is isovalent, there are no additional ligand-field d-d transitions, and there are no added unpaired electrons to complicate the optical or magnetic properties of the system. Important is that the bond connectivity is scantly disrupted; pure $ZnWO_4$ crystallizes in the nondistorted monoclinic space group $P2/c$, and it displays a direct band gap of 3.4 eV. Notably, this material acts as an excellent UV photocatalyst for organic dye degradation,[3,4] and has recently been used as a host system for increased visible-light photocatalysis.[5] The compound has been shown to be doped with transition-metal and rare-earth ions, and these doped congeners have found application in upconversion luminescence and scintillators.[6]

The first row d-block tungstates, AWO_4, (A = Mn, Fe, Co, Ni, Cu, Zn) all crystallize in the wolframite structure, which makes these materials an ideal tunable platform whose properties can be exploited through forming solid solutions. In previous work, the series, $Zn_{1-x}Cu_xWO_4$ ($0 \leq x \leq 1$) prepared by direct precipitation has been determined to be a solid solution through crystallographic analysis using high-resolution Guinier powder X-ray diffraction[7] and by Rietveld analysis of the neutron diffraction pattern.[8,9] One highlight in this phase transition is the symmetry change of the crystal from $P2/c$ to $P\bar{1}$ due to Jahn–Teller distortion of the Cu^{2+} cation. This transition is described as a ferroelastic transition, and is dependent on temperature and composition and has been modeled in terms of Landau theory using spontaneous strain to measure the order parameter.[10]

The magnetic properties of $CuWO_4$[11−13] and of the $Zn_{1-x}Cu_xWO_4$ series[14] have been investigated experimentally, and this system changes from an ordered antiferromagnet to a

Received: July 23, 2012
Published: September 7, 2012

   dx.doi.org/10.1021/ic301607g | Inorg. Chem. 2012, 51, 10394–10401

simple paramagnet as Zn^{2+} is substituted beyond the composition $Zn_{0.2}Cu_{0.8}WO_4$. $CuWO_4$ shows both long-range and short-range order that has been explained in a spin dimer analysis of the zigzag CuO_4 chains.[15] In this manuscript, we reveal the structure, magnetic properties, and optical properties of the *entire composition range* of $Zn_{1-x}Cu_xWO_4$ through X-ray diffraction, UV−vis spectroscopy, far-IR spectrosocpy, and magnetic susceptibility. The band gap decreases monotonically from 3.4 to 2.25 eV as x increases, and far-IR spectroscopy shows an approximate site symmetry change around the d-block metal cation from C_2 to C_i, apparent in the peak splitting first observed in $Zn_{0.7}Cu_{0.3}WO_4$. Magnetically, all compounds show a magnetic moment consistent with $S = 1/2$ Cu^{2+}, but the Weiss constant distinguishes the solid solutions from a two-phase mixture; it increases linearly in magnitude from −39 to −152 K as x increases. Two ordering events are observed for $CuWO_4$: a higher temperature transition at 82 K and a Néel point at 23.5 K; the higher temperature ordering disappears as x decreases below 0.8; the Néel temperature decreases from 23.5 K to 5.5 K. Most important, we use the observed changes in magnetic properties to demonstrate that the products of our modified Pechini method are solid solutions, and not phase segregated $ZnWO_4$−$CuWO_4$ mixtures after annealing.

EXPERIMENTAL SECTION

ZnO, CuO, and WO_3 starting materials were purchased from Sigma Aldrich (>99%) and used as received. $Zn_{1-x}Cu_xWO_4$ ($0 \le x \le 1$) powders were prepared by solid state methods. Eight mmol of each W and A (A = Zn, Cu) were ground in an agate mortar and pestle, pressed into a pellet, and annealed in an alumina crucible at 850 °C for 12 h, with heating and cooling ramp times of 4 h. After annealing, the samples were reground and reannealed. This process was repeated once more for a total annealing time of 36 h at 850 °C. The initial ratios of Cu:Zn were controlled to give the desired composition in the entire $Zn_{1-x}Cu_xWO_4$ series (x = 0, 0.1, 0.2, 0.3, 0.4, 0.5, 0.6, 0.7, 0.8, 0.9, and 1).

Select compounds in the series were also synthesized by a Pechini-type citric acid sol−gel method. This synthesis was adapted from a method used to prepare rare-earth metal tungstates,[16] where the optimal molar ratio of citric acid to total metal cations was 1:1, and the citric acid to ethylene glycol ratio was 2:1. In a given experiment, 2 mmol of $A(NO_3)_2{\cdot}xH_2O$ (A = Zn, Cu) and 2 mmol W from ammonia metatungstate were dissolved in 4 mmol of citric acid (3 M stock solution) and mixed with 2 mmol ethylene glycol. This solution was stirred and heated at 80−90 °C until the water evaporated, leaving a puffed gel. This gel was subsequently dried overnight in a vacuum oven at 60−70 °C. Finally, the dried gel was ground in an agate mortar and pestle and annealed at 700 °C for 3 h, with 2 h heating and cooling rates.

X-ray diffraction patterns were recorded on a Brüker D8 Advance diffractometer equipped with a graphite monochromator, a Lynx-Eye detector, and parallel beam optics using Cu−Kα radiation (λ = 1.54184 Å). Patterns were collected using a 0.6 mm incidence slit, with a step size and scan rate of 0.04°/step and 0.5 s/step respectively. The phases were identified and indexed according to the reported crystal structure determined by Schofield et al. for the $Zn_{1-x}Cu_xWO_4$ series.[7] UV−vis spectra were recorded using an Agilent-Cary 5000 spectrophotometer equipped with a Praying Mantis diffuse reflectance accessory. $BaSO_4$ was used as a baseline and samples were collected in a 1 cm diameter holder. In a measurement 50 mg of sample was diluted with 50 mg of $BaSO_4$ and packed on top of a $BaSO_4$ base to form a smooth surface flush with the holder. Spectra were recorded in reflectance mode and transformed mathematically into normalized absorbance. Tauc plots were then generated using the Kubelka−Munk function, $F(R) = (1-R)^2/2R$. Scanning electron microscopy (SEM) images were collected using a Hitachi S-3200N SEM with an accelerating voltage of 15 kV. Higher resolution SEM images were collected using a FEI Nova Nanolab SEM/FIB with an accelerating voltage of 10 kV. Inductively coupled plasma-atomic emission spectrometry (ICP-AES) elemental analysis for Cu, Zn, and W was obtained using a Perkin-Elmer Optima 2000DV instrument, and sample prep was performed using a method described by Montini et al.[17] Initially, 12 mg of material was mixed into 1 mL of 30% H_2O_2 (Fisher), 0.8 mL of HNO_3 (69% Fisher), and 1 mL of H_2O. The samples were then stirred and heated to 80 °C for 30 min and then cooled. This process was repeated, adding H_2O_2 and heating, until all materials were dissolved. As H_2O_2 was decomposed at high temperatures, H_2WO_4 began to precipitate out of solution, in which case more H_2O_2 was added to redissolve the H_2WO_4. Finally, the samples were diluted to 50 mL for storage with 1 mL extra H_2O_2 being added to prevent any precipitation. The emission lines used are 324.752 nm, 202.548 nm, and 239.708 nm for Cu, Zn, and W, respectively.

Susceptibility measurements were performed on a Quantum Design MPMS-XL7 equipped with an Evercool Dewar. About 100 mg of sample was suspended in ∼100 mg of eicosane (>99% Sigma-Aldrich) in a polycarbonate capsule. Measurements were collected under zero-field cooled conditions with a measuring field of 1 T in the temperature range 5−300 K to ensure sufficient signal-to-noise with magnetically dilute samples. The molar susceptibility was checked at lower measuring fields for the high Cu-containing materials for comparison, and the data are identical (vide infra). For each direct current (dc) susceptibility data point, the average of three measurements of 32 scans over a 4 cm scan length was acquired. Data were corrected for the diamagnetism of the sample holder and eicosane, as well as for core diamagnetism using Pascal's constants. Susceptibility data were fit to the Curie−Weiss law for $T \ge 150$ K: $\chi_M = C/(T - \Theta)$ where C relates to the effective magnetic moment as $\mu_{eff} = 2.82\ C^{1/2}$. Alternating current (ac) susceptibility measurements were recorded under an ac field $H_{ac} = H_0 \sin(2\pi ft)$ for H_0 = 3 Oe and $f \sim$ 2, 20, 200, and 1500 Hz.

RESULTS

Synthesis, Structure, and Morphology. The $Zn_{1-x}Cu_xWO_4$ series has been synthesized by traditional solid methods at 850 °C for 36 h as per the reaction:

$$x\mathrm{CuO} + (1-x)\mathrm{ZnO} + \mathrm{WO_3} \rightarrow \mathrm{Zn_{1-x}Cu_xWO_4} \qquad (1)$$

Annealing temperatures ≥850 °C have been used to synthesize $CuWO_4$, $ZnWO_4$, and other rare earth metal tungstates by traditional solid state methods.[18,19] Intermediate grinding helps to ensure complete homogenization into a single phase, which we affirm by the indexed X-ray diffraction patterns illustrated in Figure 1. Of particular note, the diffraction patterns do not change after the second 12 h annealing for any samples with one exception, x = 0.2. This composition is close to $Zn_{0.78}Cu_{0.22}WO_4$, where the transition between the monoclinic $P2/c$ structure of $ZnWO_4$ and the triclinic $P\bar{1}$ of $CuWO_4$ is observed. For the materials prepared by the Pechini method according to the overall reaction (after annealing)

$$12\mathrm{A^{2+}}(aq) + \mathrm{H_2W_{12}O_{40}^{6-}}(aq) + 8\mathrm{H_2O}(l) \rightarrow 12\mathrm{AWO_4}(s) + 18\mathrm{H^+}(aq) \qquad (2)$$

Long heating times are not required to homogenously distribute Zn^{2+} and Cu^{2+} ions since this synthesis uses soluble aqueous precursors. One 3-h annealing at 700 °C is sufficient to obtain phase pure material (Supporting Information, Figure S1).

Compound purity is verified by ICP-AES analysis on the digested samples; data are presented in Table 1. Figure 1 presents the diffraction data for the solid-state synthesized series in the range 14−27° 2θ. Notably, the Bragg reflections

dx.doi.org/10.1021/ic301607g | Inorg. Chem. 2012, 51, 10394−10401

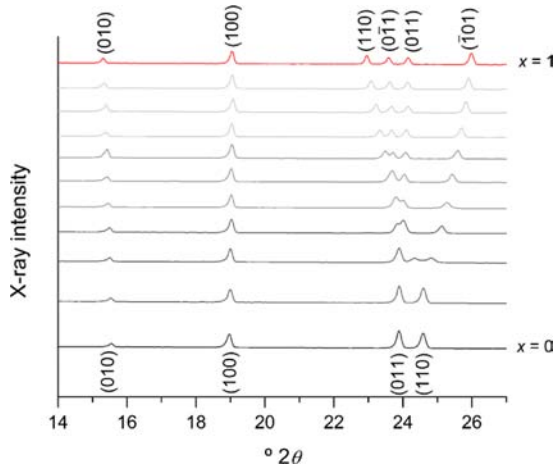

Figure 1. Indexed XRD patterns of $Zn_{1-x}Cu_xWO_4$ prepared by solid-state methods.

Table 1. ICP-AES Data for the $Zn_{1-x}Cu_xWO_4$ Series

x	Cu/mol	Zn/mol	W/mol
0	0	1	0.98
0.1	0.091	0.909	0.99
0.2	0.185	0.815	0.98
0.3	0.279	0.721	1.01
0.4	0.373	0.627	1.01
0.5	0.471	0.529	1.03
0.6	0.572	0.428	1.05
0.7	0.676	0.324	1.05
0.8	0.787	0.213	1.06
0.9	0.896	0.104	1.08
1.0	1	0	1.01

corresponding to the (010) and (100) planes do not change as a function of x. These planes are predominately related to the WO_6 octahedra, and therefore are not expected to change. Between 23 and 26° 2θ, we observe the evolution of the desymmetrization of the structure as Cu^{2+} is incorporated. The end-member composition $CuWO_4$, crystallizes in the lower symmetry $P\bar{1}$ space group, evidenced by the appearance of additional (0−11) and (−101) Bragg reflections. The (110) and (011) planes are predominately associated with the CuO_6 octahedra, and are therefore most influenced in the transition from $ZnWO_4$ to $CuWO_4$. The (110) and (011) reflections shift from 24.5 to 23.0° 2θ and from 23.9 to 24.1°2θ, respectively.

SEM images of the $Zn_{1-x}Cu_xWO_4$ series are presented in Supporting Information, Figure S2. The average particle sizes for $CuWO_4$ and $ZnWO_4$ samples are approximately 5 and 1.5 μm, respectively, for compounds prepared by solid-state reaction 1. Here, there is a gradual increase in particle size as x increases in the annealed samples. In contrast, materials prepared by the Pechini method in reaction 2 show a more uniform particle size of ∼200 nm.

Optical Properties. Figure 2 shows absorbance as a function of wavelength for the series. The end member $ZnWO_4$ shows an absorption attributed to the O(2p) → W(5d) LMCT edge at ∼425 nm. In contrast, the $CuWO_4$ absorption edge begins at 550 nm as a result of a Cu(3d) → W(5d) MMCT, with localized Cu d-d transitions observed at ∼625 nm and extending to longer wavelengths. Other compositions within the $Zn_{1-x}Cu_xWO_4$ series show absorption edges between those observed for the end member

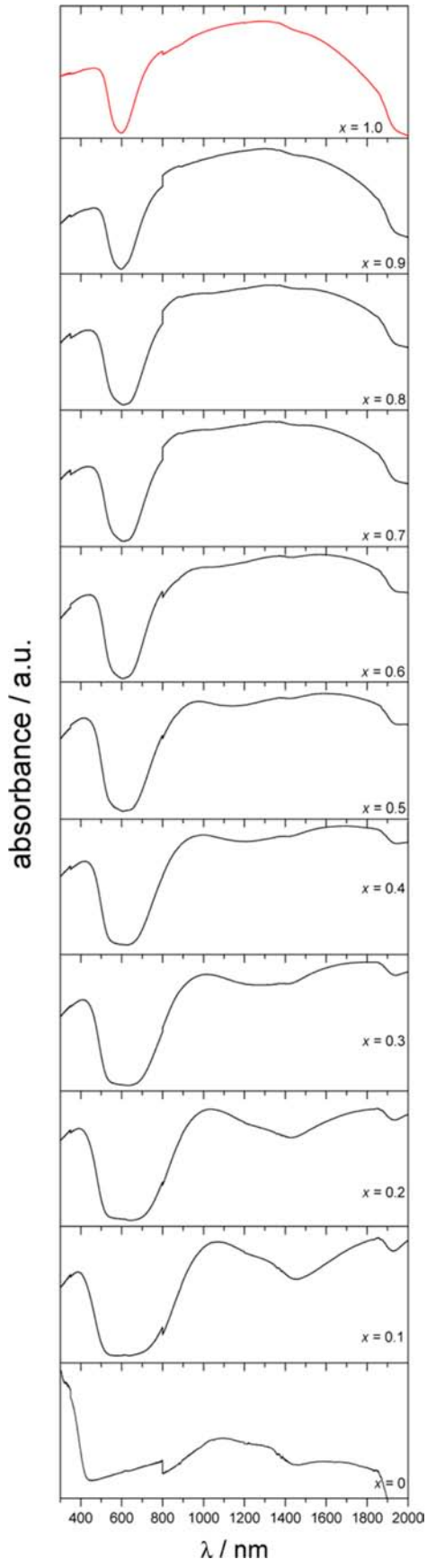

Figure 2. UV−vis−NIR spectra of the $Zn_{1-x}Cu_xWO_4$ series.

dx.doi.org/10.1021/ic301607g | Inorg. Chem. 2012, 51, 10394−10401

compositions $ZnWO_4$ and $CuWO_4$. Recent density functional theory (DFT) work suggests that Cu(3d) states contribute to the top of the valence band.[20−22] Therefore as x increases, we observe a bathochromic shift in the characteristic charge-transfer absorption edge due to increasing Cu(3d) density near the top of the valence band. Additionally, as x increases, a hypsochromic shift and concomitant increase in the intensity of the Cu d-d transitions is observed. $ZnWO_4$ and $CuWO_4$ are described as direct and indirect absorbing materials respectively; therefore we present a plot of band gap, E_g vs x in Figure 3. Both the direct and the indirect fits to the band gap decrease

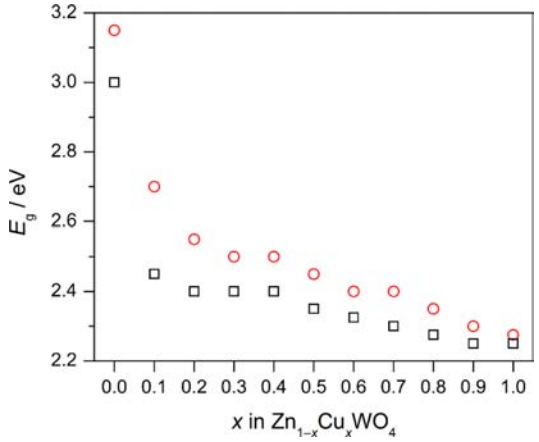

Figure 3. Direct (red circles) and indirect (black squares) band gap energies in the $Zn_{1-x}Cu_xWO_4$ series.

linearly as x increases from to 0.1 to 1, illustrating that the intermediate compositions are composed of a random distribution of Cu and Zn on the cation sublattice, and are not simply a two-phase mixture of $CuWO_4$ and $ZnWO_4$. The individual Tauc plots from which the data in Figure 3 is derived are shown in Supporting Information, Figure S3.

Far Infrared Spectroscopy. The far-IR spectra are presented in Figure 4. The $Zn_{1-x}Cu_xWO_4$ series is presented in the figure, and the data are stacked for clarity. We identify the vibrational frequencies of the M^{2+}−O (M = Cu, Zn)

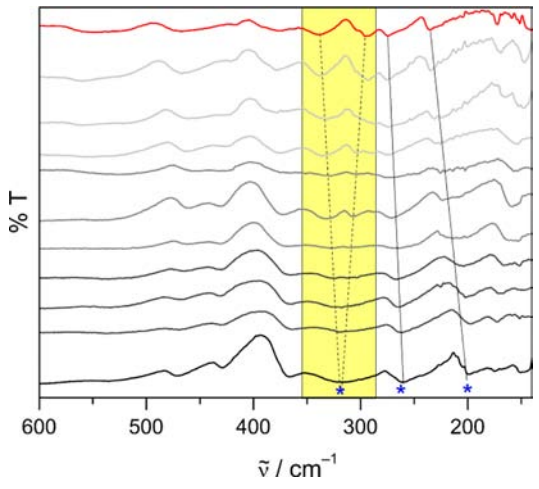

Figure 4. Far IR spectra of the $Zn_{1-x}Cu_xWO_4$ series. $ZnWO_4$ is shown in black; $CuWO_4$ is shown in red. The highlighted area shows the evolution of the A_u symmetry mode as the structure evolves from $P2/c$ ($ZnWO_4$) to $P\bar{1}$ ($CuWO_4$).

stretches by comparing the end members to known literature[23−25] and evaluating the smooth transition from $ZnWO_4$ to $CuWO_4$ throughout the series. The symmetry of these systems is reduced because the divalent cation is off-centered within the M−O octahedra.[8] Two medium-intensity Zn−O stretches in the $ZnWO_4$ structure appear at 200 cm^{-1} (B_u) and 260 cm^{-1} (B_u) and show a shift to higher energy as x increases; the lines in the figure are guides to the eye. In $CuWO_4$, the corresponding stretches are observed at 235 and 275 cm^{-1}, respectively. The highlighted region of the figure shows that the strong-intensity A_u mode in $ZnWO_4$ observed at 320 cm^{-1} splits into two peaks at x = 0.3. In $CuWO_4$, the two stretches appear at 295 and 338 cm^{-1}. The intensity and shape of the peaks in $ZnWO_4$ and $CuWO_4$ match that which has been discussed in the literature.[23] As the peaks at 200 and 260 cm^{-1} undergo a hypsochromic shift with increasing x, there is no real change in their shape, whereas the broad peak originally found at 320 cm^{-1} splits into two medium-intensity peaks found at 295 and 338 cm^{-1} in $CuWO_4$. In $CuWO_4$, the peaks at 235, 275, and 295 cm^{-1} are described as medium intensity, and the peak at 338 cm^{-1} is stronger intensity. There are also symmetric oxygen-based A_u stretches uniting W−O octahedra in the zigzag chain at 425 and 470 cm^{-1} as well as tungsten-based low energy stretches at 150 and 170 cm^{-1} that again, do not shift significantly as x changes. Our results are similar to what has been described in the compound $Zn_{0.75}Cu_{0.25}WO_4$, where low temperature mid-IR studies highlight the $P\bar{1}$ to $P2/c$ phase transition as a function of temperature.[26]

Magnetic Properties. The dc susceptibility data for the series $Zn_{1-x}Cu_xWO_4$ are shown in Figure 5. The end-member

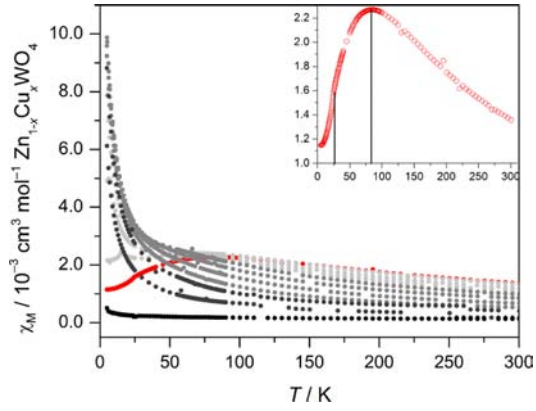

Figure 5. Molar susceptibility of the $Zn_{1-x}Cu_xWO_4$ series. $ZnWO_4$ is shown in black, $CuWO_4$ is shown in red, and intermediate compositions are in gray. **Inset** magnifies the $CuWO_4$ data and shows two ordering transitions.

composition $CuWO_4$ shows a broad peak maximum at 82 K. Ac susceptibility experiments show no frequency-dependence in this maximum (Supporting Information, Figure S4 ruling out spin glass or spin liquid behavior associated with this transition). As the concentration of copper decreases, this transition temperature decreases to 69 K (x = 0.9) and to 59 K (x = 0.8). For compositions having x < 0.8, no discernible transition is observed. To obtain sufficient signal for these magnetically dilute samples, a strong measuring field (1 T) is required. Supporting Information, Figure S5 shows that for $CuWO_4$, there are no differences in the magnetic susceptibility arising from a 1 T measuring field compared to a more typical 1000 Oe (0.1 T) measuring field.

dx.doi.org/10.1021/ic301607g | Inorg. Chem. 2012, 51, 10394−10401

Various physical methods have been employed to determine the Néel temperature of $CuWO_4$, which is elusive by simple susceptibility measurements since there is no sharp maximum in $\chi_M(T)$. The disappearance of the ($^1/_2$ 0 0) magnetic Bragg reflection in $CuWO_4$ at 23 K using neutron diffraction is definitive, and matches the temperature at which an electron paramagnetic resonance (EPR) signal disappears (24 K).[11,12] Although there is no such defining feature for T_N in the $\chi_M(T)$ plot, the first derivative $d\chi_M/dT$ shows a maximum at 23.5 K, which compares favorably to a T_N of 22.5 K reported by this method in the literature.[13] Then, the upturn in $\chi_M(T)$ below 3 K is ascribed to ferromagnetic interactions between Cu^{2+} ions within the same chemical cell, a common interaction observed for the first-row transition-metal tungstates (A = Fe, Co, Ni).[27] T_N was also determined from $d\chi_M/dT$ for x = 0.9 and 0.8: 14.5 K, and 5.5 K, respectively. The derivative plots, $d\chi_M/dT$ are presented in Supporting Information, Figure S6 for both the solid-state and the Pechini synthesized compounds.

To evaluate the spin interaction between nearest-neighboring copper atoms, we performed Curie–Weiss analysis in the paramagnetic regime as described in the Experimental Section. Figure 6 shows a plot of the effective moment (μ_{eff}) and Weiss

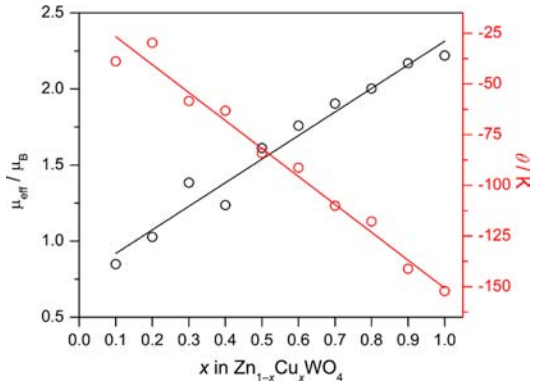

Figure 6. Trends in μ_{eff} and the Weiss constant, Θ in the series $Zn_{1-x}Cu_xWO_4$ series prepared by solid-state synthesis.

constant (Θ) as a function of x for the entire $Zn_{1-x}Cu_xWO_4$ series. The results show that the magnitude of the Weiss constant increases linearly from −39 K for x = 0.1 to −152 K for x = 1. Three effects are clear:

(1) In $CuWO_4$, there is strong antiferromagnetic coupling of nearest-neighbor spins.

(2) The variation of Θ with x reflects that the exchange interaction gets stronger as the number of paramagnetic Cu^{2+} centers increases.

(3) As expected, the effective moment increases linearly with increasing copper concentration due to incorporating greater spin density in the compound.

Then, by evaluating the magnetic moment on a per mol copper basis for each compound in the series, the average magnetic moment was found to be 2.30 ± 0.19 μ_B, which is in good agreement with the observed magnetic moment for $CuWO_4$ of 2.23 μ_B. This result is in accord with our optical data, strongly demonstrating that copper- and zinc ions statistically distribute over common 2*i* Wyckoff sites on the lattice. Accordingly, susceptibility measurements provide a method for determining whether or not a mixed-metal tungstate is in fact a solid solution or a two-compound mixture, important for the intermediate compositions here and as well as for other first row transition metal tungstates where their X-ray diffraction patterns are virtually identical because these compounds do not Jahn–Teller distort.

We have prepared $Zn_{1-x}Cu_xWO_4$ (x = 0.8, 0.9, 1.0) by a Pechini sol–gel method in which the precursors are atomically mixed prior to annealing. We focus on the compositions with high Cu^{2+} concentration here since they have the smallest band gaps. For these compounds, Supporting Information, Figure S7 compares T_N, Θ, and μ_{eff} for the compounds prepared by both methods. The $\chi_M(T)$ plots are nearly superimposable (Supporting Information, Figure S8), and the derived magnetic properties match very closely, as presented in Table 2. As in the

Table 2. Magnetic Properties of $Zn_{1-x}Cu_xWO_4$ Compounds

compound	μ_{eff}/μ_B	Θ/K	T_N/K	T_2/K	ptcl size/μm
		Solid-State Synthesis			
$CuWO_4$	2.22	−152	23.5	82	5–7
$Zn_{0.1}Cu_{0.9}WO_4$	2.17	−141	14.5	69	5–7
$Zn_{0.2}Cu_{0.8}WO_4$	2.00	−118	5.5	59	5–7
		Pechini Synthesis			
$CuWO_4$	2.26	−155	23	80	0.2–0.5
$Zn_{0.1}Cu_{0.9}WO_4$	2.16	−145	13	62	0.1–0.5
$Zn_{0.2}Cu_{0.8}WO_4$	1.99	−116	5	55	0.1–0.5

solid state preparation, T_N in materials prepared by the Pechini method decreases with decreasing copper concentration. The higher-temperature antiferromagnetic ordering transition is also observed for the Pechini compounds, and again shows a shift to lower temperature with decreasing copper content. This ordering temperature varies slightly, which may be explained by subtle differences in particle size, which has been observed in CuO nanoparticles.[28] Notably, the effective moment and Weiss constant were also determined using the paramagnetic region of the $\chi_M(T)$ plot, and match those determined for the solid-state synthesized congeners.

To provide an example of how susceptibility measurements distinguish further between having a random distribution of copper and zinc on the common 2*i* Wyckoff sites from having a two-phase mixture of $CuWO_4$ and $ZnWO_4$, we prepared a SQUID sample composed of 50% $CuWO_4$ and 50% $ZnWO_4$ by mass. The $\chi(T)$ in Figure 7 compares the gram susceptibility for the 1:1 two-phase mixture, synthesized $Zn_{0.5}Cu_{0.5}WO_4$, and pure $CuWO_4$. Of note is that the 1:1 mixture shows a

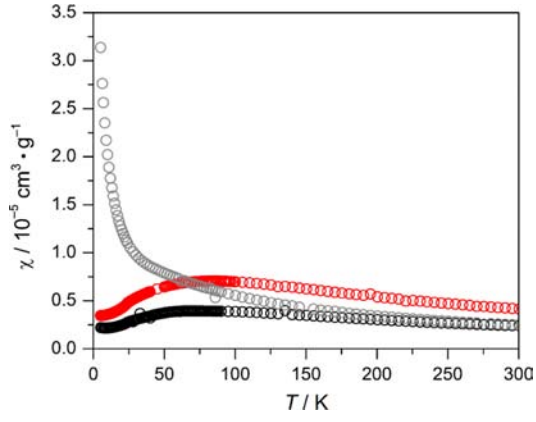

Figure 7. Comparison of the gram susceptibility of $CuWO_4$ (red), a 1:1 mixture of $ZnWO_4$:$CuWO_4$ (black), and the compound $Zn_{0.5}Cu_{0.5}WO_4$ (gray).

dx.doi.org/10.1021/ic301607g | Inorg. Chem. 2012, 51, 10394–10401

susceptibility that is ~1/2 that of $CuWO_4$, but is otherwise indistinguishable. This is expected for $CuWO_4$ buried in a diamagnetic host matrix. In contrast, the synthesized compound $Zn_{0.5}Cu_{0.5}WO_4$ is distinct; it shows no discernible magnetic transitions.

DISCUSSION

Our study is aimed at investigating the magnetic and spectroscopic properties of a magnetically dilute systems, $Zn_{1-x}Cu_xWO_4$ to correlate crystallographic data with our magnetic and spectroscopic results in potential photocatalytic materials. The first thing to note is that the magnetic structure of $CuWO_4$ is complex. At a molecular level, it is described as a spin dimer with zigzag chains of CuO_6 edge-sharing octahedra. The ordering transition we observe at 23.5 K arises from long-range 3-D antiferromagnetic ordering with a unit cell that doubles along the crystallographic a axis. Unlike most magnetically dilute system, however, the $Zn_{1-x}Cu_xWO_4$ system is intermediate between 1- and 2-dimensional systems, characterized by an ordering temperature that is no longer observed below $x = 0.8$ in $Zn_{1-x}Cu_xWO_4$. Instead, the system transforms to a simple paramagnet below $x = 0.8$.[14] However, the broad maximum in the susceptibility at higher copper concentration has been well described in the literature, and this transition increases monotonically with x. This transition at 82 K in $CuWO_4$ is attributed to the strongest antiferromagnetic interaction in $CuWO_4$, yet it does not lead to long-range ordering.[11] Rather, the high-temperature antiferromagnetic ordering above the Néel point found in $Zn_{1-x}Cu_xWO_4$ (x = 0.8, 0.9, 1) mimics the susceptibility behavior in CuO, which shows a similar type of ordering above its true Néel point.[29] This ordering has been interpreted as the transition from cooperative to noncooperative magnetism, (i.e., a transition from lattice- to molecular interactions at the Néel point) as described by Wucher.[30]

A mean field theory treatment for $CuWO_4$ gives an average exchange constant J of -213 cm^{-1} according to the equation:

$$\Theta = \frac{zJS(S+1)}{3k_B} \quad (3)$$

where z is the number of nearest neighbor spins (2 in the zigzag chains of the wolframite structure), $S = 1/2$ for Cu^{2+}, and k_B is the Boltzmann constant, 0.695 cm^{-1} K^{-1}. We note that this energy is on par with the sum of the intrachain interactions calculated by Koo and Whangbo (the sum of the exchange energies of intrachain antiferro- and ferromagnetic components in their DFT study is -282 cm^{-1}).[15] We note, however, that the analysis in reference 15 is based on a more detailed spin dimer model that also explains the short-range order at 90 K in $CuWO_4$. We point out the similarity in coupling constants simply to demonstrate that the decrease in intrachain coupling as the Zn-concentration increases in our materials may also explain that disappearance of any short-range order as x decreases.

Our studies are reminiscent of recent work regarding diamagnetic magnesium- and zinc incorporation into $MnWO_4$. These substitutions result in the destabilization of the magnetic structure, which produces a concentration-dependence for specific antiferromagnetic ordering events as well as the dielectric permittivity.[33] Further studies into this system show the formation of a robust ferroelectric state in $Mn_{0.95}Zn_{0.05}WO_4$ through suppressing the frustrated para-electric low-temperature phase as well as the magnetic, thermodynamic, and dielectric properties in $Mn_{1-x}Zn_xWO_4$ (x = 0–0.5).[34] The influence of diamagnetic Zn^{2+} ions substituting for Cu^{2+} in $Zn_{1-x}Cu_xWO_4$ (x = 0.8–1) also shows a decrease in T_N and suppression of the higher temperature ordering even with increasing x, which has been previously examined[14] and matches our quantified results. In general, it has been shown that doping into $MnWO_4$ with both diamagnetic ions such as Zn^{2+} and Mg^{2+}, as well as paramagnetic ions such as Fe^{2+} and Co^{2+} influences the ordering temperatures found within the host system: simply, diamagnetic ions decrease the ordering temperatures while paramagnetic ions increase the ordering temperatures.[31−39]

The observed changes in both the high-temperature transition and the Néel temperature for $Zn_{1-x}Cu_xWO_4$ (x = 0.8, 0.9, 1) are consistent with a magnetic Ising model.[40] Specifically, Néel points in Mn-, Fe-, and $CuWO_4$ shift to lower temperatures as described by these theories.[14,31] Interestingly, because of the complex magnetic properties of $CuWO_4$, it shows deviation from the ideal models using 1- or 2-dimensional systems in that the transition from an antiferromagnetically ordered material to a simple paramagnet occurs at such low dilution.

Our results have direct implication in understanding the electronic structure of water-oxidation photoanodes that our group has prepared. Our highest performing (i.e., highest current) photoanodes are composed of a 1:1 mixture of wolframite $CuWO_4$ and monoclinic WO_3, whose structure and composition we conclude by X-ray diffraction and elemental analysis. To understand how electronic structure impacts the kinetics on the $CuWO_4$ for water oxidation, the $Zn_{1-x}Cu_xWO_4$ series will provide insight into the charge transport limitations of this system by incorporating a closed shell 2+ cation which does not contain potential trap states that arise at a bulk heterojunction as is the case in our $CuWO_4$:WO_3 composite materials. Moreover, the optical data provides insight into the electronic structure of $Zn_{1-x}Cu_xWO_4$. Our results indicate a smooth transition in the series, with a subtle crystallographic phase change at $x = 0.20$ due to Jahn–Teller distortion of Cu^{2+}. Since the crystallographic, magnetic, and vibrational modes change with composition in a smooth manner, we assume that the band structure follows suit. As more copper is incorporated into the structure, the greater the Cu(3d) density contributes to the top of the valence band. This raises the potential energy of the valence band, thereby lowering the overall band gap. Additionally, it has been shown that the W(5d) band edges differs in $CuWO_4$ (+0.4 V vs RHE) and $ZnWO_4$ (−0.4 V), which has substantial consequences for the electronic structure in terms of photocatalytic water splitting. $ZnWO_4$ is capable of overall water splitting due to its O(2p) based valence band maximum located at about +3.0 V, and its conduction band minimum at −0.4 V. $CuWO_4$ has a band structure that is not capable of overall water splitting, but its valence band edge positioned at +2.6 V allows for greater catalytic performance in the visible part of the spectrum. The interplay between band edge positions (overpotential), band gap (photon flux), and bandwidth (carrier mobility) determines the rate in photo-catalysis, and this forms the basis of ongoing experiments in our laboratory.

Of course, the differences in the electronic structures of $CuWO_4$ and $ZnWO_4$ arise because of their d-electron counts, d^9 and d^{10}, respectively. Jahn–Teller distorted Cu^{2+} has a singly occupied $d_{x^2-y^2}$ orbital that can act as a trap state, diminishing

dx.doi.org/10.1021/ic301607g | Inorg. Chem. 2012, 51, 10394–10401

the bulk conductivity. Yet, the strong absorption edge in the visible afforded by adding Cu(3d) character to the top of the valence band is necessary for getting efficient visible-light absorption. Therefore, the interplay between photon absorption and charge separation will dictate the optimal photocatalytic chemistry such as water oxidation or dye degradation.[41,42] Additionally, the fact that this is a true solid solution makes incorporating other first-row visible-light absorbing transition metal tungstates including Mn, Fe, Co, and Ni a feasible endeavor.[43] The wolframite structure is typical of first row transition metals, and the larger band dispersion in wolframite compared to schellite (the other common tungstate crystal structure) results in a smaller effective mass, leading to higher charge carrier mobility.[19,44] Finally, we can use $ZnWO_4$ as a host material because its catalytic activity under UV illumination is quite high in comparison to the other UV light harvesting tungstates.[45]

CONCLUSIONS

We have prepared the series of compounds $Zn_{1-x}Cu_xWO_4$ by two different methods: an established solid-state synthesis and a modified Pechini synthesis. We have characterized the structural, optical, and magnetic properties in the full composition range to distinguish between generating a two-phase mixture of paramagnetic $CuWO_4$ embedded in a diamagnetic $ZnWO_4$ matrix from preparing the single-phase material, $Zn_{1-x}Cu_xWO_4$. X-ray diffraction and far-IR spectroscopy support a smooth change in structure as Zn^{2+} substitutes for Cu^{2+}, with a band gap that decreases monotonically as the Cu^{2+} content increases. The effective moment (μ_{eff}) is commensurate with $S = 1/2$ Cu^{2+} for all compositions, and the magnitude of the Weiss constant (Θ) increases as x increases, further supporting a smooth transition from $ZnWO_4$ to $CuWO_4$ as x changes. In contrast, a 1:1 $CuWO_4$:$ZnWO_4$ physical mixture shows magnetic ordering that is identical to that of $CuWO_4$. Therefore, as research progresses, this $Zn_{1-x}Cu_xWO_4$ platform will be suitable to evaluate the interplay between the band gap energy and charge transfer kinetics in visible light photocatalysis.

ASSOCIATED CONTENT

Supporting Information

SEM images, Tauc plots of UV−vis data, ac susceptibility of $CuWO_4$, and $\chi_M(T)$ plots of materials prepared by the Pechini method. This material is available free of charge via the Internet at http://pubs.acs.org.

AUTHOR INFORMATION

Corresponding Author

*Fax +01-734-647-4865. Phone: +01-734-615-9279. E-mail: bartmb@umich.edu.

Notes

The authors declare no competing financial interest.

ACKNOWLEDGMENTS

We thank the University of Michigan for generous start-up funding. We thank the Department of Chemistry for a Robert W. Parry spring/summer research fellowship for J.E.Y. and for a summer undergraduate research fellowship for J.B.K. SQUID magnetometry instrumentation at the University of Michigan was funded by the NSF MRI program (CHE-1040008). SEM instrumentation at the University of Michigan Electron Microbeam Analysis Laboratory was funded by NSF Grant DMR-0320740.

REFERENCES

(1) Yourey, J. E.; Bartlett, B. M. *J. Mater. Chem.* **2011**, *21*, 7651.
(2) Yourey, J. E.; Kurtz, J. B.; Bartlett, B. M. *J. Phys. Chem. C* **2012**, *116*, 3200.
(3) Fu, H.; Lin, J.; Zhang, L.; Zhu, Y. *Appl. Catal., A* **2006**, *306*, 58.
(4) Fu, H.; Chengsi, P.; Zhang, L.; Zhu, Y. *Mater. Res. Bull.* **2007**, *42*, 696.
(5) Su, Y.; Zhu, B.; Guan, K.; Gao, S.; Lv, L.; Du, C.; Peng, L.; Hou, L.; Wang, X. *J. Phys. Chem. C* **2012**, *116* (34), 18508−18517.
(6) Bonanni, M.; Spanhel, L.; Lerch, M.; Fuglein, E.; Muller, G. *Chem. Mater.* **1998**, *10*, 304.
(7) Schofield, P. F.; Redfern, S. A. T. *J. Phys.: Condens. Matter* **1992**, *4*, 375.
(8) Redfern, S. A. T.; Bell, A. M. T.; Henderson, C. M. B.; Schofield, P. F. *Eur. J. Mineral.* **1995**, *7*, 1019.
(9) Schofield, P. F.; Knigh, K. S.; Redern, S. A. T.; Cressey, G. *Acta Crystollogr.* **1997**, *B53*, 102.
(10) Redfern, S. A. T. *Phys. Rev. B* **1993**, *48*, 5761.
(11) Anders, A. G.; Avyagin, A. I.; Kobets, M. I.; Pelikh, L. N.; Khats'ko, E. N.; Yurko, V. G. *Sov. Phys.-JETP* **1972**, *35*, 934.
(12) Forsyth, J. B.; Wilkinson, C.; Zvyagin, A. I. *J. Phys.: Condens. Matter* **1991**, *3*, 8433.
(13) Ehrenberg, H.; Theissmann, R.; Gassenbauer, Y.; Knapp, M.; Wltschek, G.; Weitzel; Fuess, H.; Herrmanndörfer, T.; Sheptyakov, D. *J. Phys.: Condens. Matter* **2002**, *14*, 8573−8581.
(14) Zvyagin, A. I.; Anders, A. G. *Sov. Phys.-JETP* **1974**, *40*, 154.
(15) Koo, H.-J.; Whangbo, M.-H. *Inorg. Chem.* **2001**, *40*, 2161.
(16) Galceran, M.; Pujok, M. C.; Aguiló, M.; Díaz, F. *J. Sol-Gel Sci. Technol.* **2007**, *42*, 79.
(17) Montini, T.; Gombac, V.; Hameed, A.; Felisari, L.; Adami, G.; Fornasiero, P. *Chem. Phys. Lett.* **2010**, *498*, 113.
(18) Tomaszewicz, E.; Worztynowicz, A.; Kaczmarek, S. M. *Solid State Sci.* **2007**, *9*, 43.
(19) Kim, D. W.; Cho, I.-S.; Shin, S. S.; Lee, S.; Noh, T. H.; Kim, D. H.; Jung, S.; Hong, K. S. *J. Solid State Chem.* **2011**, *184*, 2103.
(20) Khyzhun, O. Y.; Bekenev, V. L.; Solonin, Y. M. *J. Alloys Compd.* **2009**, *480*, 184.
(21) Lalić, M. V.; Popović, Z. S.; Vukajlović, F. R. *Comput. Mater. Sci.* **2011**, *50*, 1179.
(22) Lalić, M. V.; Popović, Z. S.; Vukajlović, F. R. *Comput. Mater. Sci.* **2012**, *63*, 163.
(23) Clark, G. M.; Doyle, W. P. *Spectrochim. Acta* **1966**, *22*, 1441.
(24) Fomichev, V. V.; Kondratov, O. I. *Spectrochim. Acta* **1994**, *50A*, 1113.
(25) Ruiz-Fuertes, J.; Errandonea, D.; Locomba-Perales, R.; Segura, A.; Gonzalez, J.; Rodriquez, F.; Manjon, F. J.; Ray, S.; Rodriguez-Hernandez, P.; Munoz, A.; Zhu, Zh.; Tu, C. Y. *Phys. Rev. B* **2010**, *81*, 2241145.
(26) Redfern, S. A. T. *Phys. Rev. B* **1993**, *48*, 5761.
(27) Wilkinson, C. *Acta Crystallogr., Sect. A* **1973**, *29*, 449.
(28) Punnoose, A.; Magnon, H.; Seehra, M. S.; Bonevich, J. *Phys. Rev. B* **2001**, *64*, 174420.
(29) O'Keeffe, M.; Stone, F. S. *J. Phys. Chem. Solids* **1962**, *23*, 261.
(30) Wucher, J. *Acad. Sci. Paris* **1955**, *241*, 288.
(31) Obermayer, H. A.; Dachs, H.; Schröcke, H. *Solid State Commun.* **1973**, *12*, 779.
(32) Wegner, F. *Solid State Commun.* **1973**, *12*, 785.
(33) Meddar, L.; Josse, M.; Deniard, P.; La, C.; Andre, G.; Damay, F.; Petricek, V. *Chem. Mater.* **2009**, *21*, 5203.
(34) Chaudhury, R. P.; Ye, F.; Fernandez-Baca, J. A.; Lorenz, B.; Wang, Y. Q.; Sun, Y. Y.; Mook, H. A.; Chu, C. W. *Phys. Rev. B* **2011**, *83*, 014401.
(35) Ye., F.; Ren, Y.; Fernandez-Baca, J. A.; Mook, H. A.; Lynn, J. W.; Chaudhury, R. P.; Wang, Y.-W.; Lorenz, B.; Chu, C. W. *Phys. Rev. B* **2008**, *78*, 193101.

(36) Chaudhury, R. P.; Ye., F.; Fernandez-Baca, J. A.; Wang, Y.-W.; Sun, Y. Y.; Lorenz, B.; Mook, H. A.; Chu, C. W. *Phys. Rev. B* **2010**, *82*, 184422.
(37) Chaudhury, R. P.; Lorenz, B.; Wang, Y.-Q.; Sun, Y. Y.; Chu, C. W. *New J. Phys.* **2009**, *11*, 033036.
(38) Song, Y. S.; Chung, J. H.; Park, J. M. S.; Choi, Y. N. *Phys. Rev. B* **2009**, *79*, 224415.
(39) Bahoosh Golrokh, S.; Wesselinowa, J. M. *J. Appl. Phys.* **2012**, *111*, 083906.
(40) Oguchi, T.; Obokata, T. *J. Phys. Soc. Jpn.* **1969**, *27*, 1111.
(41) Irie, H.; Watanabe, Y.; Hashimoto, K. *J. Phys. Chem. B* **2003**, *107*, 5483.
(42) Huang, G.; Shi, R.; Zhu, Y. *J. Mol. Catal. A: Chem.* **2011**, *348*, 100.
(43) Lacomba-Perales, R.; Ruiz-Fuertes, J.; Errandonea, D.; Martínez-Garcia, D.; Segura, A. *Europhys. Lett.* **2008**, *83*, 37002.
(44) Ouyang, S.; Kikugawa, N.; Chen, D.; Zou, Z.; Ye, J. *J. Phys. Chem. C* **2009**, *113*, 1560−1566.
(45) Fu, H.; Pan, C.; Zhang, L.; Zhu, Y. *Mater. Res. Bull.* **2007**, *42*, 696.